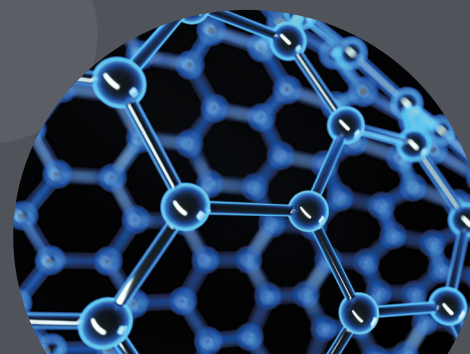
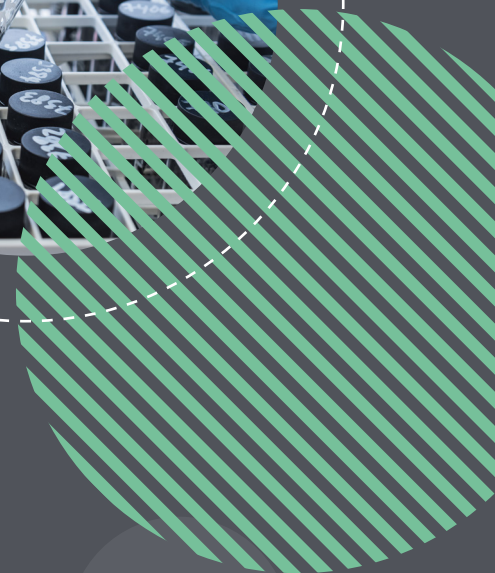
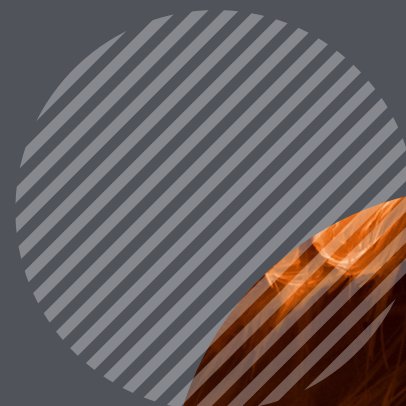




EDINBURGH
INSTRUMENTS

Nanocarbon & 2D Materials

eBook Series



edinst.com

Contents

Rapid Excitation Emission Matrix Analysis of Single Wall Carbon Nanotubes - FLS1000	3
Raman Microscopy of Graphene - RM5	6
High-Resolution Raman & Photoluminescence Imaging of MoS ₂ - RM5	10
Second Harmonic Generation Microscopy - RMS1000	13
Multimodal Imaging of CVD Grown WSe ₂ – RMS1000	15

Rapid Excitation Emission Matrix Analysis of Single Wall Carbon Nanotubes - FLS1000

Key Highlights

- SWCNTs are highly tuneable and can be tailored for specific applications
- Chiral indexes provide information on the electronic properties
- Excitation emission matrix spectroscopy is used to identify chiral structures
- Rapid SWCNT characterisation with NIR camera

Rapid Excitation Emission Matrix Analysis of Single Wall Carbon Nanotubes

Using excitation emission matrix spectroscopy, in this application note the FLS1000 Photoluminescence Spectrometer, equipped with an InGaAs NIR camera, is used to identify the chiral indexes present in a SWCNT sample.

Single-wall carbon nanotubes (SWCNTs) have unique electrical, thermal, mechanical, and optical properties which make them attractive for a wide variety of applications; ranging from drug delivery to battery electrodes. SWCNTs can be envisaged as a graphene layer that has been rolled up into a cylinder with different tube structures possible depending on how the graphene layer is rolled. The tube diameter and chirality (orientation of the graphene lattice with respect to the tube axis) are defined by the roll-up vector shown in Figure 1 as a red arrow. The roll-up vector magnitude and angle are described by a pair of integers (n , m) called the chiral index.

SWCNTs are interesting because their electronic properties heavily depend on the

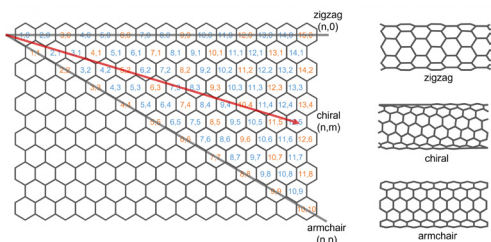


Figure 1: Roll-up vector of SWCNTs and chiral indexes. Blue chiral indexes have semiconducting properties while the orange are metallic.

chiral index of the tube structure. SWCNTs with chiral indexes coloured in orange in Figure 1 exhibit metallic properties while those in blue are semiconducting, with the bandgap varying with chiral index. This gives SWCNTs a wealth of tunability and their properties can be tailored to specific applications. Many SWCNT synthesis methods result in a mixture of chiral structures and identifying the chiral structures present in a synthesised sample is therefore vital. One of the most powerful methods for SWCNT identification is photoluminescence spectroscopy. In this application note, the FLS1000 Photoluminescence Spectrometer equipped with an InGaAs NIR camera is used to identify the chiral indexes present in a SWCNT sample using excitation emission matrix spectroscopy.

Experimental Setup

SWCNTs were synthesised using the HiPCo process and dispersed in an aqueous surfactant solution at a concentration of 0.01 mg ml^{-1} (NanoIntegris, NanoGauge IsoTubes-S). The photoluminescence of the SWCNT solution was measured using an Edinburgh Instruments FLS1000 Photoluminescence Spectrometer equipped with a double excitation monochromator and an emission spectrograph with an InGaAs NIR camera. 3 ml of the SWCNT solution was pipetted into a quartz cuvette and held in the N-J03 Front Face Sample Holder.

Excitation Emission Matrix Acquisition

A SWCNT sample contains a multitude of tube structures with different chiral indexes and therefore different bandgaps. The SWCNTs in the sample will therefore

have a range of absorption bands and to fully characterise the photoluminescence properties of all semiconducting SWCNTs present, an excitation emission matrix (EEM) is required. In an EEM, the photoluminescence spectrum is measured as a function of excitation wavelength to build a 3D fingerprint of all semiconducting SWCNT structures present in the sample. To measure EEMs quickly the acquisition time of each photoluminescence spectrum should be as short as possible. To enable the rapid measurement of NIR EEMs the FLS1000 can be equipped with an InGaAs NIR camera which captures the entire NIR spectrum in a matter of seconds.

Using the FLS1000's Fluoracle® software, an automated EEM was set up. The excitation wavelength was varied between 250 nm and 850 nm with 2 nm steps and the excitation intensity was corrected using the FLS1000's reference detector. The photoluminescence emission was measured between 900 nm and 1400 nm in a single capture using the InGaAs NIR camera. The EEM of the SWCNT sample is shown in Figure 3 with a total acquisition time of 30 minutes.



Figure 2: FLS1000 Photoluminescence Spectrometer.

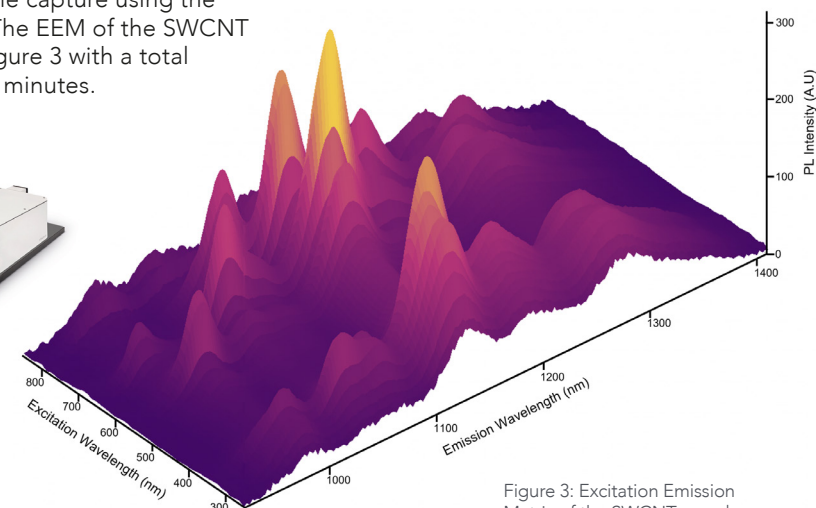


Figure 3: Excitation Emission Matrix of the SWCNT sample.

The excitation emission matrix is shown as a colour plot in Figure 4b where two emissive regions are highlighted. The low wavelength excitation region marked in blue corresponds to $v_3 \rightarrow c_3$ absorption followed by $c_1 \rightarrow v_1$ photoluminescence while the region at higher excitation wavelengths marked in green corresponds to $v_2 \rightarrow c_2$ absorption followed by $c_1 \rightarrow v_1$ photoluminescence. For identification of the SWCNT structures the $v_2 \rightarrow c_2$ region marked in green is most often used.

Empirical relationships between the E_{11} and E_{22} transition energies and the chiral indexes of the SWCNT structures were established by Bachilo et al.¹ The energies of the E_{11}

(emission) and E_{22} (excitation) transitions in wavenumber units (cm^{-1}) are given by:

$$E_{11} = \frac{1 \times 10^7 \text{ cm}^{-1}}{157.5 + 1066.9 d_t} + \frac{A_1 \cos(3\alpha)}{d_t^2}$$

$$E_{22} = \frac{1 \times 10^7 \text{ cm}^{-1}}{145.6 + 575.7 d_t} + \frac{A_2 \cos(3\alpha)}{d_t^2}$$

where A_1 and A_2 are constants that depend on the chiral index (n, m) of the SWCNT structure:

$$\text{For } (n - m) \bmod 3 = 1 \quad A_1 = -710 \text{ cm}^{-1} \quad A_2 = 1375 \text{ cm}^{-1}$$

$$\text{For } (n - m) \bmod 3 = 2 \quad A_1 = 369 \text{ cm}^{-1} \quad A_2 = -1475 \text{ cm}^{-1}$$

and d_t and α are the SWCNT tube diameter and chiral angle respectively which can be calculated from the chiral indexes and the carbon-carbon bond distance $a_{c-c} = 0.144 \text{ nm}$:

$$d_t = \frac{\sqrt{3} a_{c-c}}{\pi} \sqrt{n^2 + nm + m^2}$$

$$\alpha = \arctan\left(\frac{m\sqrt{3}}{2n + m}\right)$$

For example, a SWCNT structure with a chiral index of (7,6) has E_{11} and E_{22} transition energies of approximately 8900 cm^{-1} and $15,440 \text{ cm}^{-1}$ respectively. Converting to wavelength, this corresponds to a peak in the EEM at an emission wavelength (λ_{11}) of 1120 nm and excitation wavelength (λ_{22}) of 648 nm. Using this methodology, the peaks in the EEM can be assigned to specific SWCNT structures as shown in Figure 5. The intensity of the photoluminescence peaks provides information on the relative concentration of the nanotube structures present in the sample and it can be seen from Figure 4 that this sample has an abundance of 9,4 and 7,6 structures. Hence, by using EEM analysis researchers

can fully characterise the distribution of semiconducting nanotube structures present in a synthesised SWCNT sample.

Conclusion

Excitation emission matrix spectroscopy with the FLS1000 Photoluminescence Spectrometer was used to identify the chiral structures present in a SWCNT sample. NIR EEMs of SWCNTs can be measured rapidly with an FLS1000 equipped with an InGaAs NIR camera.

References

1. Sergei M. Bachilo, Michael S. Strano, Carter Kittrell, Robert H. Hauge, Richard E. Smalley & R. Bruce Weisman, Structure-Assigned Optical Spectra of Single-Walled Carbon Nanotubes, *Science*, 2002, 298, 2361-2366

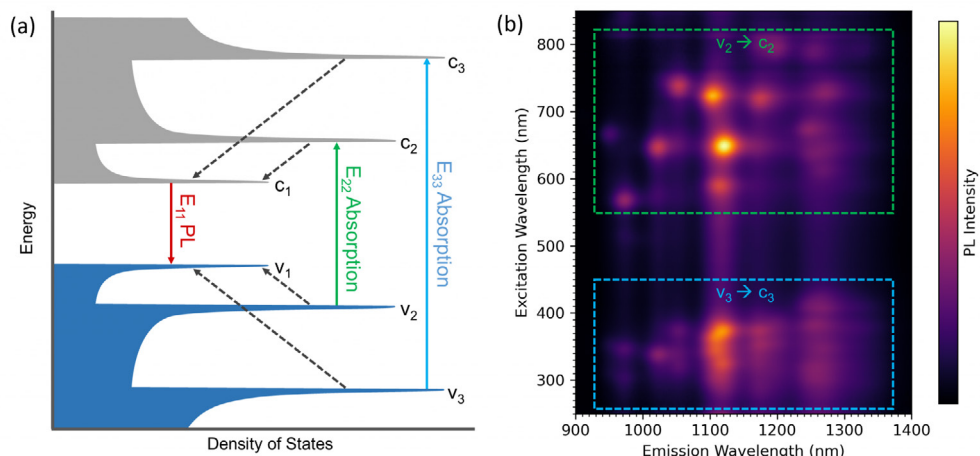


Figure 4: (a) Schematic density of states of a single SWCNT structure. The valence band is coloured in blue and the conduction in grey. Solid arrows are optical transitions between the valence and conduction bands and dashed arrows are non-radiative intraband relaxation between the band levels. Adapted from Bachilo et al.¹ (b) EEM map of the SWCNT sample showing the two emissive regions corresponding to $v_3 \rightarrow c_3$ absorption followed by $c_1 \rightarrow v_1$ emission (blue) and $v_2 \rightarrow c_2$ absorption followed by $c_1 \rightarrow v_1$ emission (green).

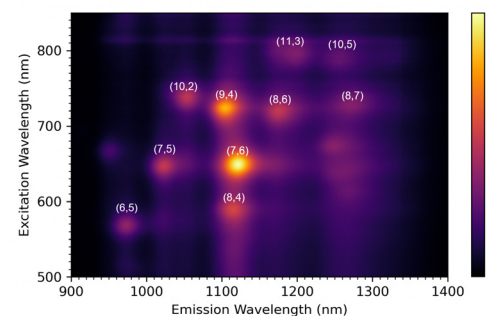


Figure 5: Identified SWCNT structures from the excitation emission matrix.

Raman Microscopy of Graphene - RM5

Key Highlights

- Raman microscopy reveals the quality of deposited graphene layers
- Layer number determination via 2D- and G-Band
- Strain determination via G-Band
- Defect mapping via D-Band

Raman Microscopy of Graphene

Introduction

First reported in Science in 2004, graphene is commonly termed the “wonder material” due to its impressive properties.¹ Geim and Novoselov, the two scientists behind the first isolation of graphene, were awarded the 2010 Nobel Prize in Physics for their pioneering research into graphene.

Graphene is the thinnest material known to exist, whilst also being extremely strong – around 200 times stronger than steel. Graphene is an excellent conductor of electricity and heat as is optically transparent. The applications of graphene are extensive, and include energy storage, photodetectors, and computer chips.

The structure and bonding of graphene make it well suited for Raman spectroscopy. Graphene is one atom thick carbon; the carbon atoms are arranged in a hexagonal lattice. The sp^2 carbon bonds result in highly polarisable π bonds which give an intense Raman signal. This is because the vibrational mode is “Raman active” and this occurs when the molecular polarisability changes during the vibration. Raman spectroscopy can be used in the evaluation of graphene quality and thickness. Since Raman microscopy is non-destructive and has high spatial and spectral resolution, the technique is well-suited for gathering detailed information about the graphene film.^{2,3} There is also minimal or no sample preparation required for Raman

spectroscopy, further adding to its ease of use and low damage risk. In this application note, an Edinburgh Instruments RM5 Raman Microscope is used to highlight how Raman microscopy an essential tool for any material scientist researching graphene.

Materials and Methods

An RM5 Raman Microscope equipped with a 532 nm laser and 1200 gr/mm grating was used to investigate three graphene samples: monolayer, bilayer, and trilayer graphene on a silicon substrate. Since graphene is an incredibly thin material, care must be taken with Raman spectroscopy to avoid laser induced heating in the sample. The RM5 has fully automated laser attenuators, controlled via the Ramacle[®] software, allowing the user to ensure no laser damage occurs to the sample.

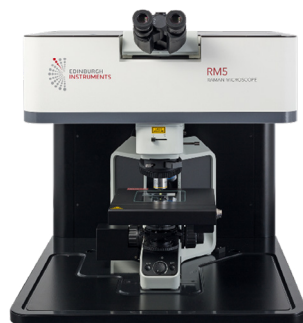


Figure 1: Edinburgh Instruments RM5 Raman Microscope.

Results and Discussion Raman Spectra of Graphene

There are 3 main bands of interest in the Raman spectra of graphene, Figure 2, the G-band, the D-band, and the 2D-band. These bands are indicative of the number of layers

of graphene present and the quality of the sample. Whilst the D-band and 2D-band will always be present, the D-band will only be seen for samples containing defects. These three bands will now be discussed in detail.

The spectrum in Figure 2 was measured using 532 nm excitation, you may also see 633 nm commonly employed. These lasers are most used due to the resonance between sample and excitation wavelength. Resonance Raman is an enhancement technique where the laser wavelength is chosen to be close to the frequency of an electronic transition in the sample. Due to the resonance properties for the main bands in Raman analysis of graphene, it is important to always use the same excitation wavelength when investigating samples to allow for comparisons to be made. The D-band and 2D-band, discussed in more detail below, will differ between excitation wavelengths, as shown in Figure 3. The difference is due to Double Resonance Raman scattering (DRR), which is a rare second-order 2-phonon process. DRR is dependent on the incoming excitation wavelength and thus the laser wavelength chosen affects peak positions. DRR is most observed in materials science, for example when studying MoS_2 , carbon nanotubes, and graphene.⁴

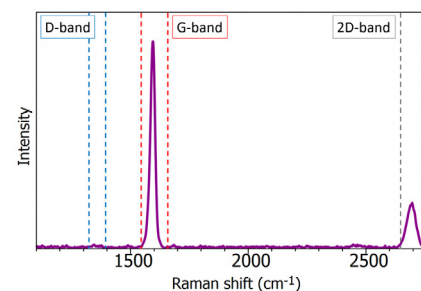


Figure 2: Raman spectrum of graphene.

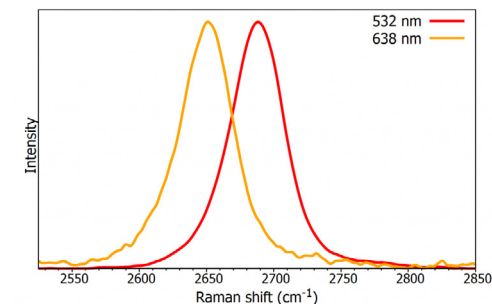


Figure 3: Normalised Raman spectra of the 2D-band from graphene excited with a 532 nm and 638 nm laser.

The G-band

The G-band is a sharp band at approximately 1585 cm^{-1} and represents the in-plane stretching vibrations of the sp^2 bonded carbon atoms. Its position is affected by the number of layers present, as shown in Figure 4, the peak shifts to lower wavenumbers as the number of graphene layers increases. This blue shift is caused by different dimer interaction as the number of layers increases. The number of layers can be calculated from the peak position using the following equation where ω_G is the band position, and n the number of layers present:⁵

$$\omega_G = 1581.6 + 11(1 + n^{1.6})$$

The spectra in Figure 4 also show the difference in G-band intensity between different layers of graphene, as the layers increase so too does the peak intensity, and this follows closely to a linear trend. Both changes in the G-band can be used to determine layer thickness, however the peak position is also sensitive to strain, temperature and doping so care needs to be taken when using this band for layer evaluation.

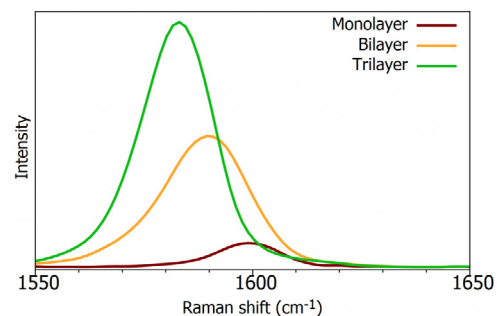


Figure 4: Raman spectra from the G-band of monolayer, bilayer, and trilayer graphene.

The 2D-band

The 2D-band (also referred to as the G'-band) is also indicative of the number of layers present in the sample. The 2D-band originates from a double resonance enhanced two-phonon lateral vibrational process.⁶ Although this band is the second order overtone of the D-band, discussed below, it does not arise from a defect and therefore is not indicative of defects.

The 2D-band changes in shape and position as the layers of graphene increase, as shown in Figure 5. The spectra have been normalised for easier comparison. This is more complicated than a simple peak shift as

seen with the G-band. Monolayer graphene has a single Lorentzian peak as there is only 1 component to the 2D-band. As the layers increase the peak broadens and changes shape. For example, the 2D-band of bilayer graphene has 4 components as there are 4 possible double resonance scattering processes, whilst there is only 1 possible for monolayer graphene. The 2D-band is also sensitive to graphene folding and this should be considered when using the band to determine layer thickness.

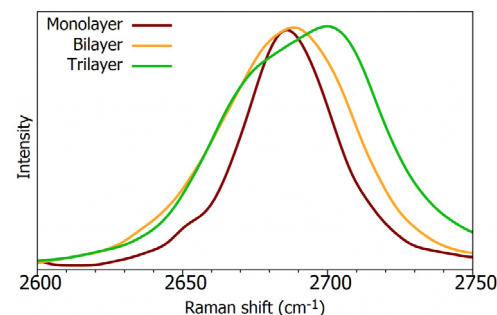


Figure 5: Normalised Raman spectra of the 2D-band of monolayer, bilayer, and trilayer graphene.

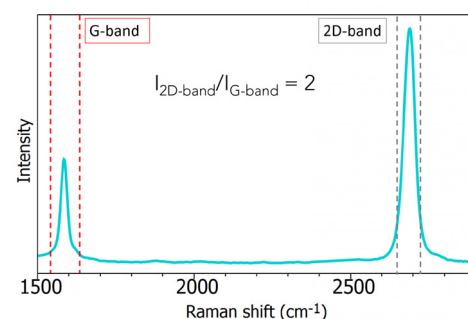


Figure 6: Single layer graphene spectrum.

The two bands discussed so far can also be used together to determine if the sample is monolayer graphene. This is by the ratio of the peak intensities. For high quality single layer graphene, the ratio of I_{2D}/I_G will be equal to 2, presented in Figure 6.

The D-band

The D-band is the peak which highlights defects in the sample, Figure 7. It can be monitored to highlight areas particularly high in defects. The more intense this band, the higher the level of disorder within the sample. It is caused by the ring breathing mode from sp^2 carbon rings and must be adjacent to a defect to be Raman active. The D-band is a 1-phonon lattice vibrational process and is a double resonance band.

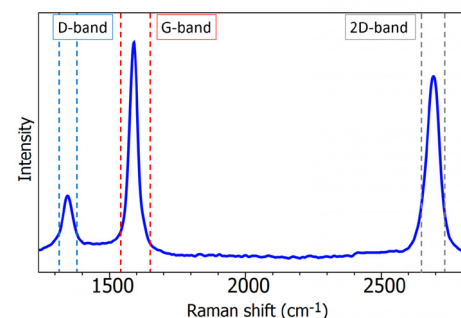


Figure 7: Raman spectrum of graphene sample containing a defect.

Raman mapping graphene samples allows the visualisation of areas particularly high in defects. The truly confocal nature of the RM5 allows for high spatial resolution which is critical for graphene analysis. Defects can include broken bonds or the presence of sp^3 bonded carbon. Figure 8a shows the reflected white light image of a graphene sample, clearly just by this image alone it is impossible to see where the defects are located. Next a Raman map was taken using a 100×0.9 N.A. objective with a $100\ \mu\text{m}$ pinhole. From the Raman map acquired the intensity of the D-band can be plotted, producing Figure 8b. The image shows areas of the graphene film high in defects.

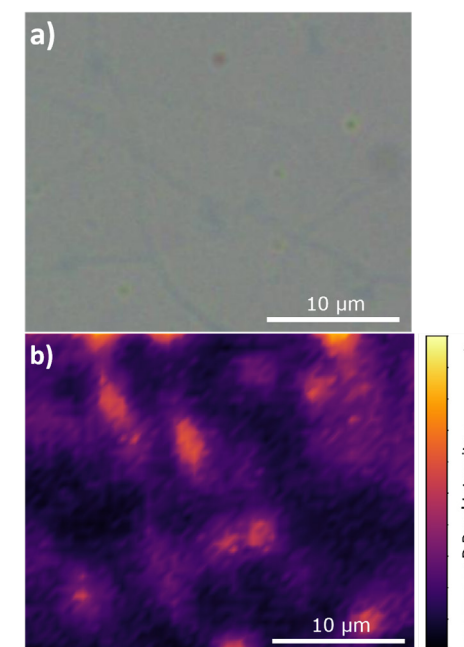


Figure 8: a) Reflected brightfield image of graphene b) Raman image highlighting areas of defects.

Conclusion

In this application note the ability of confocal Raman microscopy can be used for determining the number of layers of graphene is highlighted. Additionally, we show how Raman mapping can produce images which reveal areas of the sample which are high in disorder.

The RM5 Raman Microscope's high spatial and spectral resolution allows for high quality graphene analysis, the perfect tool for any materials scientist.

References

1. Novoselov, K. S. et al. Electric Field Effect in Atomically Thin Carbon Films Supplementary. *Science* (80) (2004)
2. Ni, Z., Wang, Y., Yu, T. & Shen, Z. Raman spectroscopy and imaging of graphene. *Nano Res* (2008)
3. Ferrari, A. C. & Basko, D. M. Raman spectroscopy as a versatile tool for studying the properties of graphene. *Nature Nanotechnology* (2013)
4. Wu, J. Bin, Lin, M. L., Cong, X., Liu, H. N. & Tan, P. H. Raman spectroscopy of graphene-based materials and its applications in related devices. *Chemical Society Reviews* (2018)
5. Wang, H., Wang, Y., Cao, X., Feng, M. & Lan, G. Vibrational properties of graphene and graphene layers. *J. Raman Spectrosc* (2009)
6. Venezuela, P., Lazzeri, M. & Mauri, F. Theory of double-resonant Raman spectra in graphene: Intensity and line shape of defect-induced and two-phonon bands. *Phys. Rev. B – Condens. Matter Mater. Phys* (2011)

High-Resolution Raman & Photoluminescence Imaging of MoS₂ – RM5

Key Highlights

- CVD-grown MoS₂
- Rapid Raman & PL Imaging using FastMAP™
- Layer number determination
- Strain localisation

High-Resolution Raman & Photoluminescence Imaging of MoS₂

Introduction

Transition metal dichalcogenides (TMDs) are a class of 2D materials which have unique optical and electronic properties. They are semiconductors with the chemical structure MX₂ where M is a transition metal and X a chalcogen, Figure 1. After the isolation of graphene layers, research into alternative 2D layered materials which offer the same, or better, properties has surged.

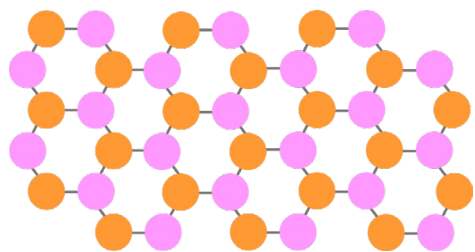


Figure 1: TMD structure MX₂; M=Transition Metal (pink) (e.g., Mo) X=Chalcogen (orange) (e.g., S)

Bulk MoS₂ has an indirect band gap, while in monolayer form the band gap becomes direct. The direct band gap is formed due to the removal of interlayer interactions meaning electrons are confined to a single plane. Mechanically MoS₂ monolayers are highly flexible, they have a higher breaking strength than commonly used flexible plastics, and stiffness comparable to steel.¹

The applications of MoS₂ are numerous and wide-ranging, with interest from fields such as optoelectronics, water treatment, solar energy, and biomedicine. For the material

to perform at its highest capability it must be defect free. Defects, stress, and strain can significantly influence the properties of the material. For example, removing defects responsible for non-radiative recombination allows photoluminescence quantum yields of over 95% to be realised.² Correlative Raman and photoluminescence (PL) imaging can be used to provide highly detailed sample information without any sample preparation or damage.

Using a confocal Raman microscope both Raman and PL maps can be obtained on the same sample area. In this Application Note, CVD-grown MoS₂ flakes are analysed using Raman and PL imaging with the RM5 Raman Microscope.

Materials and Methods

An Edinburgh Instruments RM5 Raman Microscope equipped with a 532 nm laser and two gratings; 300 gr/mm for PL and 1800 gr/mm for Raman, was used to analyse MoS₂ flakes. The MoS₂ flakes were Chemical Vapor Deposition (CVD) grown on sapphire, Figure 2.

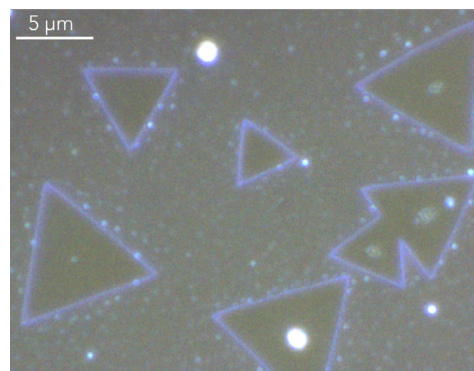


Figure 2: Reflected darkfield image of MoS₂ flakes.

The sample exhibits a strong Raman and PL response allowing short exposure times on the CCD camera to be used to obtain high quality spectra. During mapping when exposure times of < 0.5 seconds can be used, Fast Mapping is employed to greatly reduce mapping times. For Raman imaging an exposure time of 0.03 s was used, since PL was more intense 0.01 s exposure times could be used.

MoS₂ Raman Imaging

The Raman spectrum of MoS₂ consists of two characteristic bands termed the E_{2g} band at 385 cm⁻¹ and the A_{1g} band at

405 cm⁻¹, Figure 3. The E_{2g} band is due to in-plane vibrations, and the A_{1g} band attributed to out-of-plane vibrations.

These bands are indicative of the number of layers present and the number of layers present in MoS₂ crystals is critical to their function in optoelectronic devices. From Figure 4 it can be seen the E_{2g} and A_{1g} band intensity are indicative of the number of layers present, as the number of layers increases the two bands become farther apart due to inter-layer vibrations. Crystals shown in a solid single pink colour are monolayer MoS₂. While the bright spots in the centre of some of the crystals indicates the presence of multilayer MoS₂.

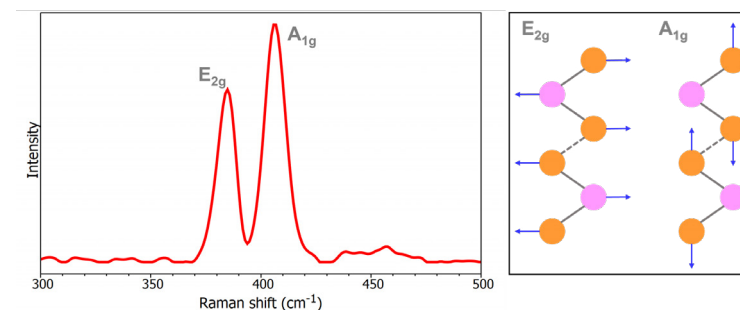


Figure 3: Raman spectrum of thin layer MoS₂ (left) highlighting the E_{2g} and A_{1g} bands and their associated vibrations (right).

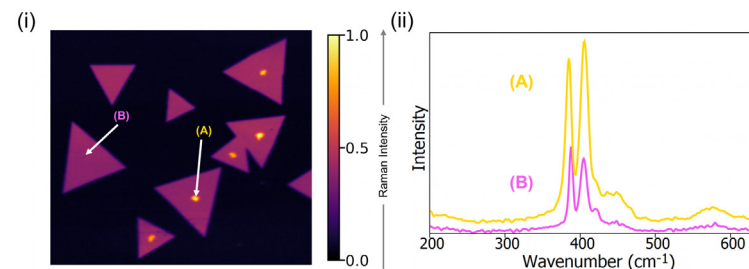


Figure 4: (i) Raman intensity imaging of MoS₂ crystals using the E_{2g} and A_{1g} bands. (ii) Raman spectra from areas of low and high Raman signal.

The splitting between the two bands was plotted, Figure 5(i). Compared to bulk MoS₂ the E_{2g} band is red shifted as the crystal becomes monolayer, this shift is due to Coulomb interactions between Mo atoms which are enhanced with increased layers.³ The A_{1g} band is blue shifted as the MoS₂ becomes monolayer, resulting in the centre of the triangles exhibiting an increased splitting value.

The E_{2g} band is particularly sensitive to strain in the sample, when under strain the band is red shifted revealing the two bottom crystals highlighted in the white box are under more strain than the others, Figure 6. Raman mapping reveals these samples contain both monolayer and multilayer MoS₂ whilst showing some strain.

MoS₂ Photoluminescence Imaging

Excitation using a 532 nm laser offers both Raman and PL signal meaning the two phenomena can be seen in a single spectrum, therefore it is technically possible to perform the two techniques simultaneously. However, to obtain the best quality spectra different gratings are used for the two measurement types. For PL imaging a low groove density grating is used to obtain the broad PL peak. The intensity of the PL band decreases with increasing layer number and bulk MoS₂ produces no PL signal at all. This effect is due to the indirect to direct band gap transition which occurs as we go from bulk MoS₂ to few-layer MoS₂. The Raman and PL intensity maps should therefore be opposites of one another when comparing areas of monolayer and multilayer MoS₂ which can be observed in Figure 7.

The PL peak is also sensitive to strain, doping, and defects, its position was plotted in Figure 8. The peak position is indicative of strain in the sample, corresponding with the E_{2g} band from Raman imaging the bottom two crystals reveal strain. Additionally, PL mapping reveals some strain in the two crystals which appear to be growing into each other, highlighted in the white box.

PL mapping offers agreement with the Raman data showing this sample has been well grown as largely monolayer crystals with little strain present.

Conclusion

This application note demonstrates how the RM5 Raman Microscope can provide high resolution imaging of 2D transition metal dichalcogenides. Raman and PL imaging can be used correlatively to gain detailed information on the sample's layers, as well as indicating strain, defects, and doping.

References

1. J. Pei *et al.*, Exciton and Trion Dynamics in Bilayer MoS₂, *Small*, 11, 6384–6390 (2015)
2. M. Amani *et al.*, Near-unity photoluminescence quantum yield in MoS₂, *Science*, 350, 1065–1068 (2015)
3. S. Golovynskiy *et al.*, Exciton and trion in few-layer MoS₂: Thickness- and temperature-dependent photoluminescence, *Appl. Surf. Sci.* 515 (2020)

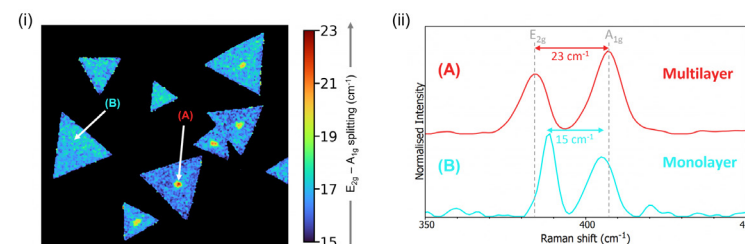


Figure 5: (i) Raman imaging displaying the band splitting of E_{2g} - A_{1g} (ii) Normalised Raman spectra from monolayer and multilayer MoS₂ highlighting the change in splitting.

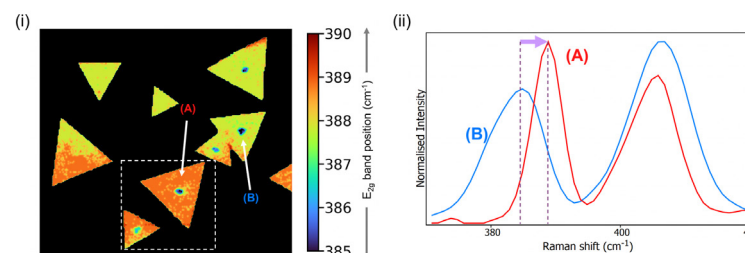


Figure 6: (i) Raman imaging displaying the band position of the E_{2g} band and (ii) Normalised Raman spectra highlighting E_{2g} band position.

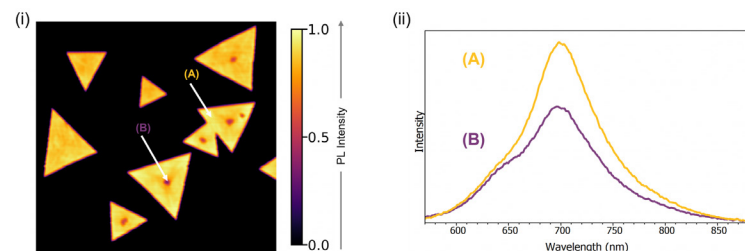


Figure 7: (i) PL intensity map of MoS₂ crystals. (ii) PL spectra from an area of high and low intensity.

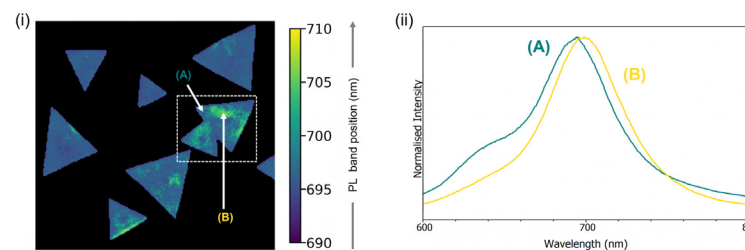
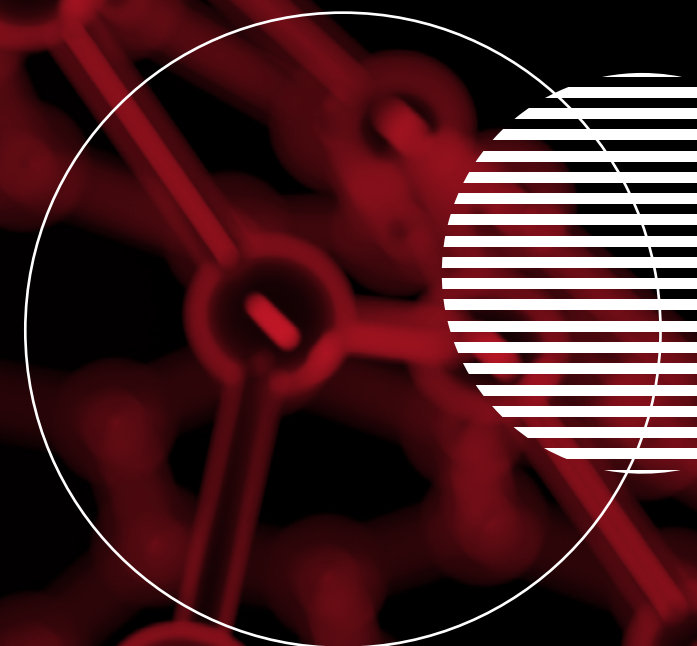


Figure 8: (i) PL imaging of MoS₂ crystals using peak position. (ii) Normalised PL spectra from an area of high and low intensity

Second Harmonic Generation Microscopy - RMS1000

Key Highlights

- Femtosecond laser can be coupled to RMS1000 for SHG Imaging
- Two photons with the same wavelength interact in the material to generate a photon with exactly half the wavelength of the incident photons
- Sensitive to the layer stacking symmetry in materials
- Used to image the grain boundaries and layer stacking in 2D semiconductors



Second Harmonic Generation Microscopy with the RMS1000 Confocal Microscope

Second Harmonic Generation Microscopy

Second harmonic generation (SHG) microscopy is an imaging technique where the sample's ability to generate second harmonic light creates contrast in the image. SHG is a non-linear optical process where two photons with the same wavelength interact in a material to generate a photon with exactly half the wavelength of the incident photons. The generation of a SHG signal depends on the symmetry of the molecular structures in present a sample, with SHG only occurring when there is a non-centrosymmetry in the excitation focal volume. This sensitivity to symmetry makes SHG imaging a powerful technique in materials science where it can be used to image the grain boundaries and layer stacking in 2D semiconductors through the changes in crystal symmetry. It can also be applied to biological tissue imaging as certain

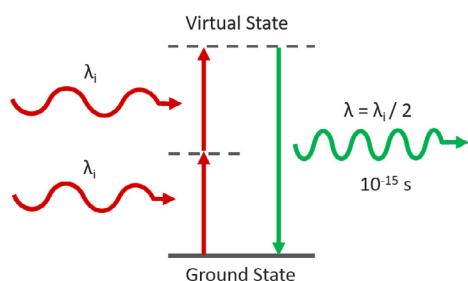


Figure 1. Second Harmonic Generation

biological tissues, such as fibrillar collagen, are non-centrosymmetric and SHG imaging is therefore highly selective towards them.

Experimental Configuration

SHG requires a very high excitation intensity which is achieved using mode-locked femtosecond pulsed lasers. Traditionally this has been titanium sapphire lasers, but femtosecond fiber lasers are becoming an increasingly attractive and economical alternative. The Edinburgh Instruments RMS1000 Confocal Raman Microscope has external laser coupling ports that enable the optical coupling of mode-locked femtosecond lasers into the microscope. An example experimental setup for SHG microscopy with the RMS1000 is shown below. The sample is excited by the femtosecond laser and the SHG signal acquired on the RMS1000 CCD camera.

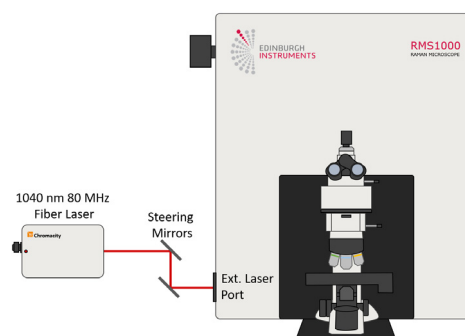


Figure 2. Example optical setup for SHG microscopy with the Edinburgh Instruments RMS1000. The laser excitation source is a Chromacity 1040 HP femtosecond fiber laser with an output wavelength of 1040 nm and a repetition rate of 80 MHz (Chromacity Ltd., UK).

Examples of SHG Imaging with the RMS1000

WSe₂ Flake

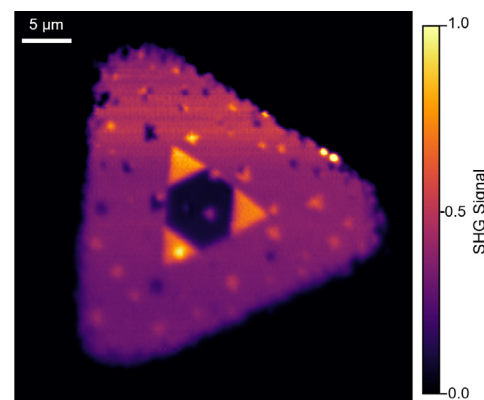


Figure 3. Second harmonic generation imaging of a WSe₂ flake grown using CVD. The SHG image reveals the presence of multiple layers in the centre of the flake. The main triangle is monolayer WSe₂ which has broken inversion symmetry (non-centrosymmetric) and therefore a SHG response. The three smaller bright triangles are bilayer WSe₂ where the second layer has the same crystal orientation as the monolayer and broken inversion symmetry is maintained and the SHG response of the layers is additive. The dark region in the centre is likely trilayer WSe₂ where the crystal growth is 180 degrees opposite to the monolayer and bilayer resulting in inversion symmetry and a significant decrease of the SHG signal.

WS₂ Polycrystal

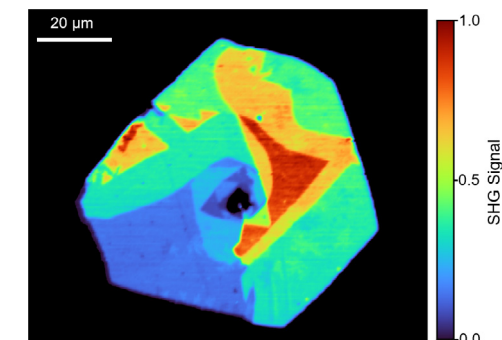


Figure 4. Second harmonic generation imaging of a WS₂ flake grown using CVD. The SHG imaging reveals that the flake is a polycrystal with each crystalline domain having a different SHG response due to differing number of layers, stacking symmetries and growth orientations.

Intestine Tissue Section

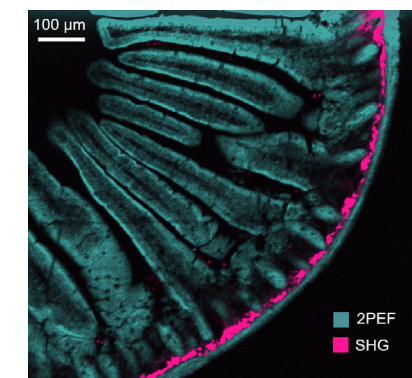
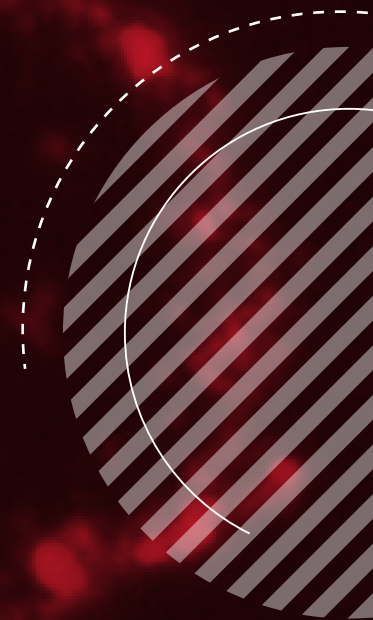


Figure 5. Second harmonic generation (SHG) and two-photon excited fluorescence (2PEF) imaging of a mouse intestine section stained with Alexa Fluor® 568. Second harmonic generation imaging setups can also be used for the complementary technique of two-photon excited fluorescence microscopy. The SHG at 520 nm and the 2PEF from the Alexa Fluor® 568 dye at 630 nm were captured simultaneously on the RMS1000 CCD camera. The SHG is from fibrillar collagen near the intestinal wall which has a strong SHG response.

Multimodal Imaging of CVD Grown WSe_2 – RMS1000



Key Highlights

- Multimodal imaging using one instrument and one software package to fully characterise layer-dependent optoelectronic properties
- Raman Imaging
- Photoluminescence Imaging
- Second Harmonic Generation Imaging

Multimodal Raman, Photoluminescence & SHG Imaging of CVD Grown WSe₂

Multimodal imaging is a powerful technique that combines two or more imaging modalities to provide a more comprehensive understanding samples. By using different types of imaging, such as Raman, photoluminescence and second harmonic generation, we can fully characterise the optoelectronic properties of samples.

Two-dimensional transition-metal dichalcogenides are a class of layered semiconducting materials that exhibit unique layer-number-dependent optical and electronic properties. In this application note, we will discuss how the RMS1000 Confocal Microscope enables multimodal imaging of tungsten diselenide (WSe₂),

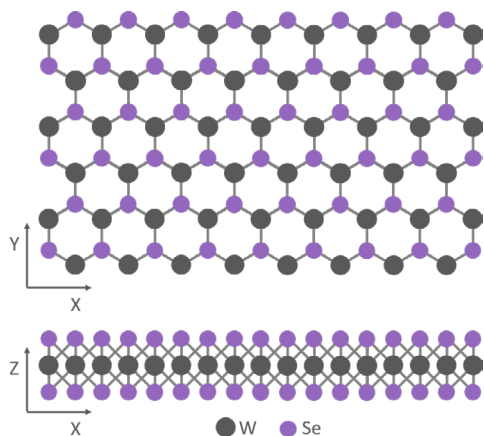


Figure 1: Monolayer WSe₂ Crystal Structure.

with five multimodal imaging options: reflected brightfield & darkfield, Raman, photoluminescence and second harmonic generation to fully characterise its layer-dependent optoelectronic properties.

Materials & Methods

WSe₂ crystals were grown on a Si substrate using chemical vapour deposition (CVD) and characterised using an Edinburgh Instruments RMS1000 Confocal Microscope. The RMS1000 was equipped with a 100x NA 0.9 objective and a back-illuminated CCD camera. For Raman and photoluminescence imaging, the WSe₂ was excited with a 532 nm laser using a 1800 gr/mm and 300 gr/mm diffraction grating to acquire the Raman and photoluminescence spectra respectively. For second harmonic generation (SHG) imaging, a Chromacity 1040 HP femtosecond fibre laser (Chromacity Ltd. UK) operating at 1040 nm and 80 MHz was coupled to the RMS1000 for excitation, and the SHG response was acquired using a 300 gr/mm diffraction grating.



Figure 2: Edinburgh Instruments RMS1000 Multimodal Confocal Microscope.

Reflected Brightfield and Darkfield Imaging

The WSe₂ crystal was first widefield imaged using reflected brightfield and darkfield (Figure 3). In the reflected brightfield image, the reflective silicon substrate appears bright and the absorbing WSe₂ crystal deposited atop is darker. Nucleation sites appear as dark spots across the crystal surface, as well as a stronger absorbing domain in the centre that is suggestive of multilayer WSe₂.

Reflected darkfield imaging provides complementary information. In darkfield, the sample is illuminated at an oblique angle and steps in sample surface height cause increased scattering and appear bright in the image. The darkfield image reveals there are two regions in the central domain with different heights, likely due to different WSe₂ layer numbers.

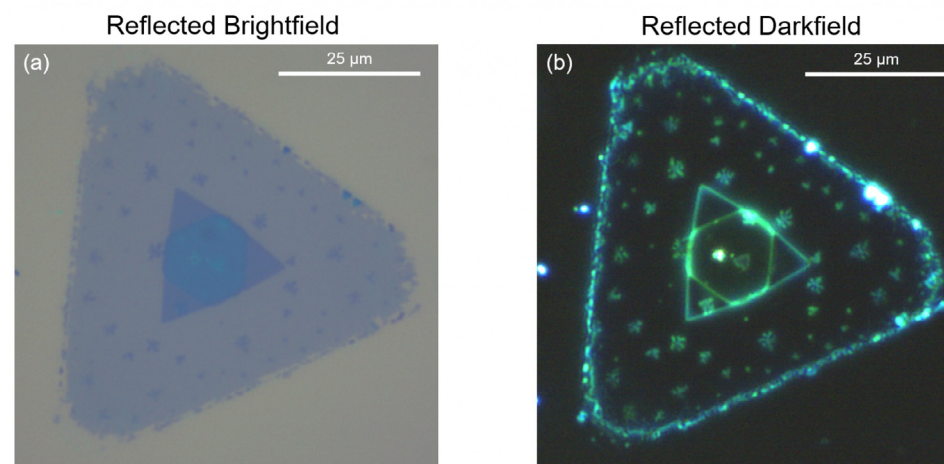


Figure 3: (a) Reflected brightfield and (b) reflected darkfield imaging of the WSe₂ crystal.

Raman Imaging

The crystal was next Raman imaged (Figure 4). WSe_2 has a characteristic Raman peak at 250 cm^{-1} (Figure 4d) which corresponds to the in-plane E_{2g}^1 and out-of-plane A_{1g} phonon modes of WSe_2 . In contrast to other transition-metal dichalcogenides, the E_{2g}^1 & A_{1g} phonon modes are almost degenerate in WSe_2 and are not individually resolved, with both contributing to the 250 cm^{-1} peak.^{1,2} In the centre of the crystal, an additional peak at 310 cm^{-1} is observed (marked with arrows in Figure 4d). This peak is symmetry forbidden in monolayer WSe_2 and indicative of multilayer WSe_2 .²

The E_{2g}^1 / A_{1g} peak intensity (Figure 4a) is highest in the large primary triangle domain, and reduces by $\sim 80\%$ within the inner triangle domain. The reduction in E_{2g}^1 / A_{1g} intensity is indicative of a change from monolayer to multilayer WSe_2 .¹ The E_{2g}^1 / A_{1g} peak position (Figure 4b) shifts from 250 cm^{-1} in the primary domain to 247 cm^{-1} within the inner domain which supports a change in layer number.³ The E_{2g}^1 / A_{1g} peak also shifts towards higher wavenumbers at the edges of the crystal which is attributed to changes in the local microenvironment at the disordered edges.

Ramacle® spectral matching analysis (Figure 4c) identified three distinct Raman spectral regions in the crystal. In spectral matching, spectra at user-selected locations in the map are designated as archetypes and the deviation of all other spectra in the map from the archetype is calculated. Lower deviations from the archetype spectra are represented by more intense colour. The monolayer WSe_2 primary domain is highlighted in blue while the inner domain was found to be composed of two regions (highlighted in red and green)

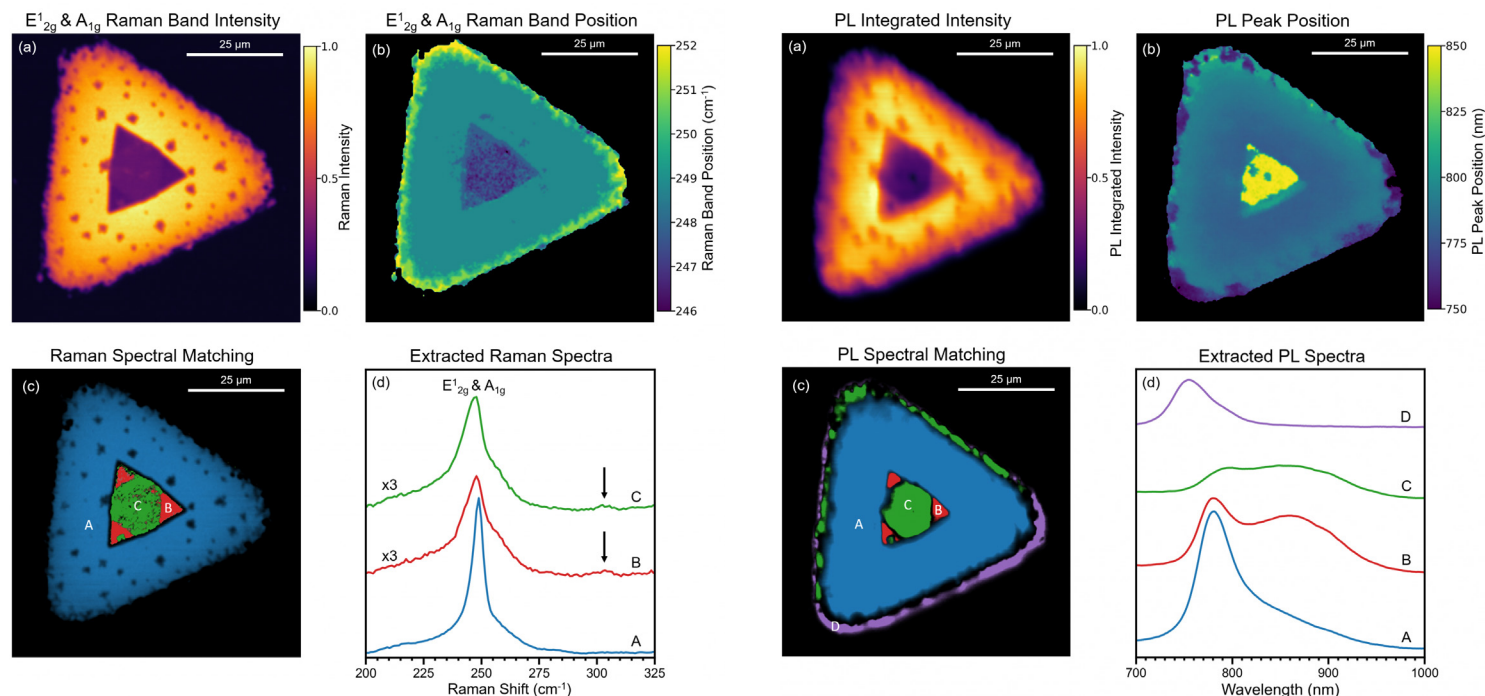


Figure 4: Raman imaging of WSe_2 . (a) Intensity of the E_{2g}^1 / A_{1g} (250 cm^{-1}) Raman band, (b) peak position of the E_{2g}^1 / A_{1g} Raman band, (c) least squares spectral matching revealing three distinct Raman spectral areas, (d) averaged Raman spectra from areas A, B and C; spectra B and C are scaled in intensity by a factor of three and the arrows mark the location of the multilayer 310 cm^{-1} peak. The Raman imaging parameters were: $40 \times 40\ \mu\text{m}^2$, 200×200 pixels, 50 ms integration time, 532 nm laser, 1800 gr/mm diffraction grating, $300\ \mu\text{m}$ pinhole.

with subtly different E_{2g}^1 / A_{1g} Raman peak shapes. This agrees with the change in surface height in the inner domain observed in the darkfield image.

Photoluminescence Imaging

To obtain additional insight into the inner domain, the crystal was photoluminescence (PL) imaged (Figure 5). The total PL intensity (Figure 5a) is lower within the inner domain, and the PL peak position (Figure 5b) red-shifted. Spectral matching (Figure 5c)

identified four distinct PL spectral regions across the crystal and their corresponding spectra are shown in Figure 5d.

Region A (blue) is monolayer WSe_2 with PL peak at 780 nm from confined exciton emission. In region B the total PL intensity is decreased with a longer wavelength shoulder peak at 870 nm , while in region C the PL intensity decreases further and spectral weight shifts to the long wavelength shoulder. It has been established that as the number of layers increases in WSe_2 ,

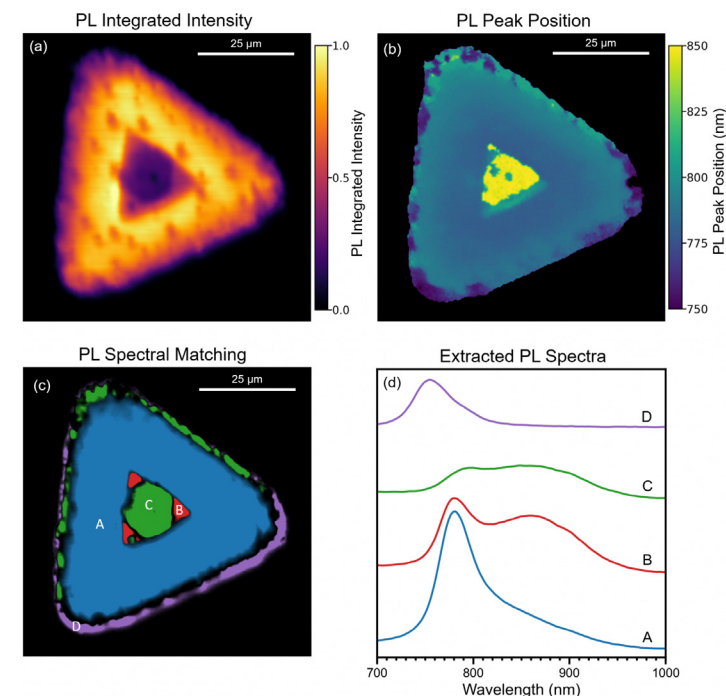


Figure 5: Photoluminescence imaging of WSe_2 . (a) Integrated intensity of the PL response, (b) PL primary peak position, (c) least squares spectral matching revealing four distinct PL spectral areas, (d) averaged PL spectra from areas A, B, C and D. The PL imaging parameters were: $40 \times 40\ \mu\text{m}^2$, 200×200 pixels, 30 ms integration time, 532 nm laser, 300 gr/mm diffraction grating, $300\ \mu\text{m}$ pinhole.

the PL emission red-shifts from exciton based emission at $\sim 1.6\text{ eV}$ ($\sim 780\text{ nm}$) in the monolayer to indirect bandgap emission at $\sim 1.2\text{ eV}$ ($\sim 1000\text{ nm}$) in bulk WSe_2 .¹ Region B and C are therefore assigned as bilayer and trilayer WSe_2 respectively. Similarly to the Raman image, significant edge effects were also observed in the PL, with the PL peak position blue-shifted on the lower edge (spectrum D) and red-shifted on the upper edge of the crystal.

Second Harmonic Generation Imaging

To determine the layer orientation within the three identified domains, the crystal was imaged using second harmonic generation (SHG) (Figure 6). SHG imaging is highly sensitive to the crystalline symmetry of transition metal dichalcogenides, with SHG only occurring when there is a non-centrosymmetry in the excitation focal volume. Monolayer WSe_2 is non-centrosymmetric and region A has a measurable SHG response as expected. The symmetry of multilayer WSe_2 depends on the type of layer stacking, 2H or 3R.⁵ In 3R stacking, each layer has the same orientation and the

multilayer is non-centrosymmetric with SHG response increasing with layer number. In contrast, in 2H stacking, each layer is rotated 180° with respect to the adjacent layers and odd-numbered multilayers are net non-centrosymmetric with an SHG response similar to the monolayer while even-numbered multilayers are net centrosymmetric with no SHG response.^{4,5}

The bilayer WSe_2 in region B has an SHG response that is twice that of the monolayer, and the two layers therefore must be 3R stacked. The trilayer WSe_2 in region C has diminished SHG response compared to the monolayer which indicates the third layer in the trilayer is rotated relative to the first and second layers resulting in a partial restoration of centrosymmetry. The blue,

red and green dashed triangles in Figure 6a illustrate the relative orientations of the three layers in the crystal. The growth of the third layer (green) has terminated at the boundaries of the second layer (red) resulting in a partial triangle.

Conclusion

Through a combination of widefield, Raman, PL and SHG imaging techniques, the layer number and stacking type in a CVD-grown WSe_2 crystal was identified. The multimodal imaging capabilities of the RMS1000 Confocal Microscope make it an ideal imaging platform for studying the optoelectronic properties of transition-metal dichalcogenides.

References

1. Toddor *et al.*, Photoluminescence emission and Raman response of monolayer MoS_2 , MoSe_2 , and WSe_2 , *Express*, 2013, 21, 4908-4916
2. Ribeiro-Soares *et al.*, Second Harmonic Generation in WSe_2 , *2D Mater.*, 2015, 2, 045015
3. Terrones *et al.*, New First Order Raman-active Modes in Few Layered Transition Metal Dichalcogenides, *Rep.*, 2014, 4, 4215
4. Zhao *et al.*, Atomically phase-matched second-harmonic generation in a 2D crystal, *Light Sci. Appl.*, 2016, 5, e16131
5. Shinde *et al.*, Stacking-controllable interlayer coupling and symmetric configuration of multilayered MoS_2 , *NPG Asia Mater.*, 2018, 10, e468

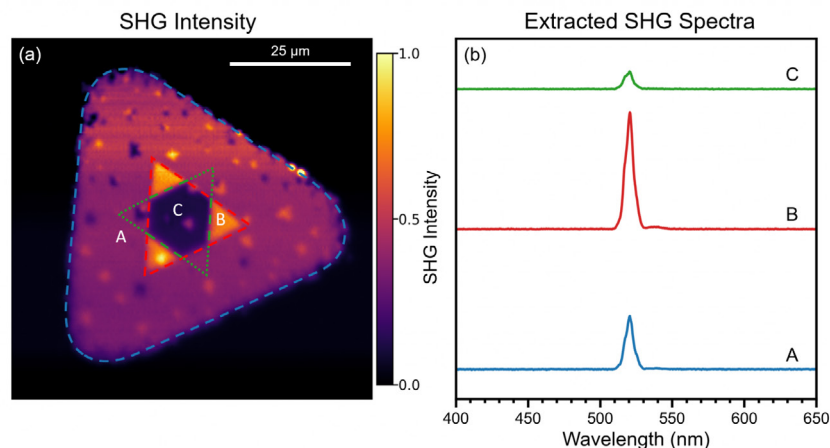


Figure 6: Second Harmonic Generation imaging of WSe_2 . (a) Intensity of the SHG peak at 520 nm. (b) extracted SHG response from areas A, B, and C. The SHG imaging parameters were: $40 \times 40 \mu\text{m}^2$, 200×200 pixels, 11 ms integration time, 1040 nm femtosecond pulsed laser, 300 gr/mm diffraction grating, 300 μm pinhole.



EDINBURGH
INSTRUMENTS

[edinst.com](https://www.edinst.com)